PARAMETER ROBUSTNESS ANALYSIS OF SYSTEM FUNCTION RECONSTRUCTION AND A NOVEL DEBLURRING NETWORK FOR MAGNETIC PARTICLE IMAGING

A THESIS SUBMITTED TO

THE GRADUATE SCHOOL OF ENGINEERING AND SCIENCE

OF BILKENT UNIVERSITY

IN PARTIAL FULFILLMENT OF THE REQUIREMENTS FOR

THE DEGREE OF

MASTER OF SCIENCE

IN

ELECTRICAL AND ELECTRONICS ENGINEERING

By

Abdullah Ömer Arol

December 2020

Parameter Robustness Analysis of System Function Reconstruction and A Novel Deblurring Network for Magnetic Particle Imaging
By Abdullah Ömer Arol
December 2020

We certify that we have read this thesis and that in our opinion it is fully adequate, in scope and in quality, as a thesis for the degree of Master of Science.

Emine Ülkü Sarıtaş Çukur(Advisor)

Tolga Çukur(Co-Advisor)

Aykut Koç

Yeşim Serinağaoğlu Doğrusöz

Approved for the Graduate School of Engineering and Science:

Ezhan Karaşan
Director of the Graduate School

ABSTRACT

PARAMETER ROBUSTNESS ANALYSIS OF SYSTEM FUNCTION RECONSTRUCTION AND A NOVEL DEBLURRING NETWORK FOR MAGNETIC PARTICLE IMAGING

Abdullah Ömer Arol
M.S. in Electrical and Electronics Engineering
Advisor: Emine Ülkü Sarıtaş Çukur
Co-Advisor: Tolga Çukur
December 2020

Magnetic Particle Imaging (MPI) is a novel medical imaging modality that can provide excellent sensitivity, contrast and resolution for imaging the spatial distribution of superparamagnetic iron oxide nanoparticles by utilizing their nonlinear magnetization responses. System function reconstruction (SFR) and x-space reconstruction are the two main image reconstruction approaches in MPI. SFR requires time-consuming calibration measurements, which need to be repeated whenever there is a change in scanning parameters or the nanoparticle. In the first part of this thesis, the effects of using mismatched parameters during calibration measurements and imaging in SFR are investigated. Through numerical simulations, MPI signals gathered with different scanning parameters are used for reconstructing images to analyze the effects of parameter changes in image quality in SFR. In contrast to the SFR approach, standard x-space reconstruction does not require calibration measurements. However, the reconstructed images are blurred by the point spread function of the system. In the second part of this thesis, a new learning-based approach is proposed to improve the image quality in x-space reconstructed images. The proposed method learns an end-to-end mapping between the x-space reconstructed blurred images and the underlying nanoparticle distributions. By using numerical simulations, it is shown that the blurring in x-space reconstruction can be significantly reduced with the proposed method.

Keywords: magnetic particle imaging, image reconstruction, system matrix, deblurring, neural networks.

ÖZET

SİSTEM FONKSİYONU GERİÇATIMI İÇİN PARAMETRE GÜRBÜZLÜK ANALİZİ VE MANYETİK PARÇACIK GÖRÜNTÜLEME İÇİN ÖZGÜN BİR NETLEŞTİRME AĞI

Abdullah Ömer Arol
Elektrik ve Elektronik Mühendisliği, Yüksek Lisans
Tez Danışmanı: Emine Ülkü Sarıtaş Çukur
İkinci Tez Danışmanı: Tolga Çukur
Aralık 2020

Manyetik Parçacık Görüntüleme (MPG) mükemmel hassasiyet, kontrast ve çözünürlük sağlayabilen yeni bir medikal görüntüleme yöntemidir. Süperparamanyetik demir oksit nanoparçacıklarının doğrusal olmayan manyetiklenme tepkilerini kullanan MPG, bu nanoparçacıkların uzaysal dağılımını görüntülemektedir. MPG'de sistem fonksiyonu geriçatımı (SFG) ve x-uzayı geriçatımı olmak üzere iki farklı görüntü geriçatım yöntemi kullanılmaktadır. SFG için uzun süren kalibrasyon ölçümleri gerekmektedir ve farklı tarama parametreleri için bu ölçümlerin tekrarlanması gerekmektedir. Bu tezin ilk bölümünde SFG'de kalibrasyon ölçümleri ve görüntüleme sırasında uyumsuz parametrelerin kullanılmasının etkileri incelenmiştir. Sayısal benzetimlerle, farklı tarama parametreleri için oluşturulmuş MPG sinyalleri kullanılarak görüntü geriçatımı gerçekleştirilmiş, ve parametre değişimlerinin SFG'de görüntü kalitesine etkisi incelenmiştir. SFG'nin aksine, standart x-uzayı geriçatımı için kalibrasyon ölçümleri gerekmemektedir, fakat sistemin nokta yayılım fonksiyonundan dolayı geriçatılan görüntüler bulanıklaşmaktadır. Bu tezin ikinci bölümünde, x-uzayı geriçatımı yöntemi ile oluşturulmuş görüntülerin kalitesini arttıracak öğrenme tabanlı yeni bir yöntem sunulmuştur. Sunulan bu yöntem x-uzayı geri çatımı ile oluşturulan bulanık görüntüler ile nanoparçacıkların uzaysal dağılımı arasındaki eşleşmeyi öğrenmektedir. Sayısal benzetimler kullanılarak x-uzayı geriçatımındaki bulanıklaşmanın, önerilen yöntem ile önemli derecede giderilebildiği gösterilmiştir.

Anahtar sözcükler: manyetik parçacık görüntüleme, görüntü geriçatımı, sistem matrisi, netleştirme, sinir ağları.

Acknowledgement

I would like to thank my advisor Assoc. Prof. Emine Ülkü Sarıtaş for her valuable advice and support during my thesis work.

I would like to thank my co-advisor Assoc Prof. Tolga Çukur and my thesis committee: Asst. Prof. Aykut Koç, Asst. Prof. Yeşim Serinağaoğlu Doğrusöz for their advice and insightful comments.

I would like to thank my friends, my colleagues and my family for their endless support.

I would like to thank the following funding agencies for supporting the work in this thesis: the Scientific and Technological Research Council of Turkey (TUBITAK 217S069) and NVIDIA Corporation (GPU grant).

Contents

List of Figures

Chapter 1

Introduction

Magnetic Particle Imaging (MPI) is a rapidly developing biomedical imaging modality that is used for estimating the spatial distribution of superparamagnetic iron oxide (SPIO) nanoparticles. MPI promises high sensitivity, high contrast, and high resolution [1, 2, 3, 4, 5]. With these capabilities, MPI has numerous applications such as angiography, multicolor imaging, stem cell tracking, and functional imaging [6, 7, 8, 9, 10, 11, 12, 13].

Two main image reconstruction methods have found widespread use in MPI. The first method, system function reconstruction (SFR), requires extensive calibration scans where a voxel-sized sample is placed one at a time at each grid point in the field-of-view (FOV) and scanned [14, 15, 16]. The second approach is called x-space reconstruction, in which the signal is first speed compensated and then directly mapped to the instantaneous position of the scanned point. This approach does not require any calibration measurements [17, 18, 19].

In SFR, calibration scans are specific to the scanner and drive field parameters, as well as the physical parameters of the magnetic nanoparticles. Changing any one of these parameters leads to the need of a new calibration scan. In Chapter 3, parameter robustness of SFR is analyzed. The effects on the reconstructed image quality for SFR are investigated for the case of changing scanning or nanoparticle parameters without performing new calibration measurements. It is shown that small changes in scanning or nanoparticle parameters do not require new calibration scans.

The main limitation of SFR is the extensive duration of the calibration scan. Although recent work has proposed methods for reducing the calibration time, the calibration scan still needs to be repeated every time there is a moderate change in scanning parameters [18, 20]. X-space reconstruction does not require any calibration measurements; however, it produces blurry images due to the point spread function of the system [17, 21]. In Chapter 4, a new learning-based reconstruction method is proposed to improve the image quality in x-space reconstruction. The proposed method is inspired by the success of neural networks in various computer vision problems. This new learning-based approach learns the mapping between x-space reconstructed blurry image and the underlying nanoparticle distribution. Furthermore, it requires fewer calibration scans when compared to the calibration measurements needed for a full system matrix in SFR.

Chapter 2

Principles of Magnetic Particle Imaging

2.1 Signal Equation

Magnetic Particle Imaging (MPI) uses the nonlinear magnetization responses of magnetic nanoparoticles (MNP), where the change in magnetization of MNPs is very small for applied magnetic fields higher than a certain threshold. Therefore, MNPs in a volume with high magnetic field have saturated magnetizations and do not respond to small variations in the applied field. MPI uses this property of MNPs to achive spatial encoding. In a MPI scanner, first an inhomogeneous magnetic field called the selection field is generated. The volume where the selection field is small is called the Field Free Point (FFP) and outside of that region is called the saturated region.

After creating the selection field, a time-varying field called the drive field is generated to excite the MNPs and move the FFP inside the scanning volume. While moving the FFP, magnetization of MNPs inside or close to the FFP will change and induce a signal on inductive receive coils. MNPs in the saturated region do not respond to the drive field, hence do not induce any signal, as explained in Figure 2.1.

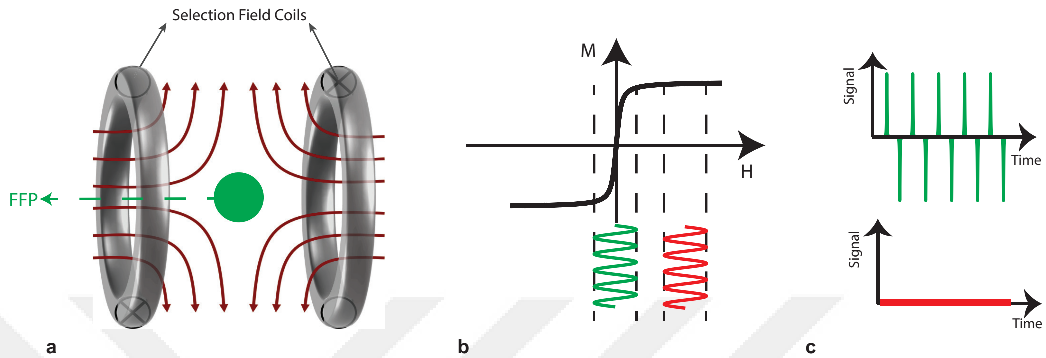

Figure 2.1: (a) Topology of a MPI scanner. The FFP is represented by the green circle, and the outside of the circle is the saturated region. (b) Magnetization curve of MNPs. Magnetization of the particles in the green region will change with drive field and generate a signal on the receive coil (c). Magnetization of the particles in the saturated region will not change with additional drive field, and hence they do not generate a signal on the receive coil.

The total magnetic field in the scanner can be expressed as the summation of the selection and drive fields as given in Equation 2.1 for the 1D case.

$$H(x,t) = H_d(t) + H_s(x) \tag{2.1}$$

Here, H_s is the static selection field and H_d is the time-varying drive field. From this equation, the location of FFP, x_s, can be obtained by finding the positions with zero magnetic field:

$$H(x_s,t) = H_d(t) + H_s(x_s) = 0 \tag{2.2}$$

$$H_s(x_s) = -H_d(t) \tag{2.3}$$

In MPI scanners, the selection field is typically generated using either two permanent magnets with identical poles facings each other, or a Maxwell coil pair. This configuration generates magnetic field with constant gradient inside the Field-of-View (FOV). By substituting H_s with a field with constant gradient $-G$, we get the following equations:

$$H_s(x) = -Gx \tag{2.4}$$

$$x_s(t) = (-G)^{-1}(-H_d(t)) \tag{2.5}$$

$$H_d(t) = Gx_s(t) \tag{2.6}$$

Then, the equation for the total magnetic field can also be expressed in terms of x_s as follows:

$$H(x,t) = H_d(t) + H_s(x) \tag{2.7}$$

$$= Gx_s(t) - Gx \tag{2.8}$$

$$H(x,t) = G(x_s(t) - x) \tag{2.9}$$

The response of MNPs to an applied magnetic field can be modelled by Equation 2.10 [17]:

$$M(H) = mc\mathcal{L}[H/H_{sat}] \tag{2.10}$$

Here, M is the magnetization of MNPs, m is the magnetic moment of MNPs, c is the concentration of MNPs, $\mathcal{L}$ is the Langevin function, and H_{sat} is the magnetic field required for saturation of MNPs.

For the 1D case, the magnetization of particles and the total flux can be expressed as:

$$M(x,t) = mc(x)\mathcal{L}[G(x_s(t) - x)/H_{sat}] \tag{2.11}$$

$$\Phi(t) = m \int c(u)\mathcal{L}[(G(x_s(t) - u)/H_{sat}]du \tag{2.12}$$

$$\Phi(t) = mc(x) * \mathcal{L}[Gx/H_{sat}]\Big|_{x=x_s(t)} \tag{2.13}$$

From the flux, the signal generated by MNPs on an inductive receive coil with sensitivity $-B_1$ can be calculated as:

$$s(t) = B_1 \frac{d\Phi}{dt} \tag{2.14}$$

$$s(t) = B_1 mc(x) * \dot{\mathcal{L}}[Gx/H_{sat}]\Big|_{x=x_s(t)} G\dot{x}_s(t)/H_{sat} \tag{2.15}$$

In this relation $\dot{\mathcal{L}}[Gx/H_{sat}]$ is the point spread function (PSF) in the 1D case. With similar derivations, the signal equation for 3D MPI can be expressed as [18]:

$$s(t) = B_1 mc(\mathbf{x}) *** \frac{||\dot{\mathbf{x}}_s||}{H_{sat}} \mathbf{h}(\mathbf{x}) \frac{\dot{\mathbf{x}}_s}{||\dot{\mathbf{x}}_s||} \Bigg|_{\mathbf{x}=\mathbf{x}_s(t)} \tag{2.16}$$

where $\mathbf{x}_s$ is the position of FFP in FOV, $\mathbf{h}$ is the 3D PSF of the MPI system. PSF of the system with magnetic field gradient matrix $\mathbf{G}$ can be expressed as [18]:

$$\mathbf{h}(\mathbf{x}) = \dot{\mathcal{L}}\left(\frac{||\mathbf{Gx}||}{H_{sat}}\right) \frac{\mathbf{Gx}}{||\mathbf{Gx}||} \left(\frac{\mathbf{Gx}}{||\mathbf{Gx}||}\right)^T \mathbf{G} + \frac{\mathcal{L}\left(\frac{||\mathbf{Gx}||}{H_{sat}}\right)}{\frac{||\mathbf{Gx}||}{H_{sat}}} \left(\mathbf{I} - \frac{\mathbf{Gx}}{||\mathbf{Gx}||} \left(\frac{\mathbf{Gx}}{||\mathbf{Gx}||}\right)^T\right) \mathbf{G} \tag{2.17}$$

Here, the PSF of the system can be separated into two components with the following envelopes [18]:

$$\mathrm{ENV}_T = \dot{\mathcal{L}}\left(\frac{||\mathbf{Gx}||}{H_{sat}}\right) \tag{2.18}$$

$$\mathrm{ENV}_N = \frac{\mathcal{L}(\frac{||\mathbf{Gx}||}{H_{sat}})}{\frac{||\mathbf{Gx}||}{H_{sat}}} \tag{2.19}$$

ENV_T is called the tangential envelope and ENV_N is called the normal envelope. As shown in Figure 2.2, the tangential envelope will have significantly reduced blurring effect when compared to the normal envelope.

In 3D x-space MPI reconstruction, depending on the FFP velocity vector, $\dot{\mathbf{x}}_s$, $\mathbf{h}$ can be decomposed into the following components:

$$\mathbf{h}_{||}(\mathbf{x}) = \hat{\mathbf{e}}_1 \cdot \mathbf{h}(\mathbf{x})\hat{\mathbf{e}}_1 \quad \text{collinear} \tag{2.20}$$

$$\mathbf{h}_{\perp,\mathbf{1}}(\mathbf{x}) = \hat{\mathbf{e}}_2 \cdot \mathbf{h}(\mathbf{x})\hat{\mathbf{e}}_1 \quad \text{transverse} \tag{2.21}$$

$$\mathbf{h}_{\perp,\mathbf{2}}(\mathbf{x}) = \hat{\mathbf{e}}_3 \cdot \mathbf{h}(\mathbf{x})\hat{\mathbf{e}}_1 \quad \text{transverse} \tag{2.22}$$

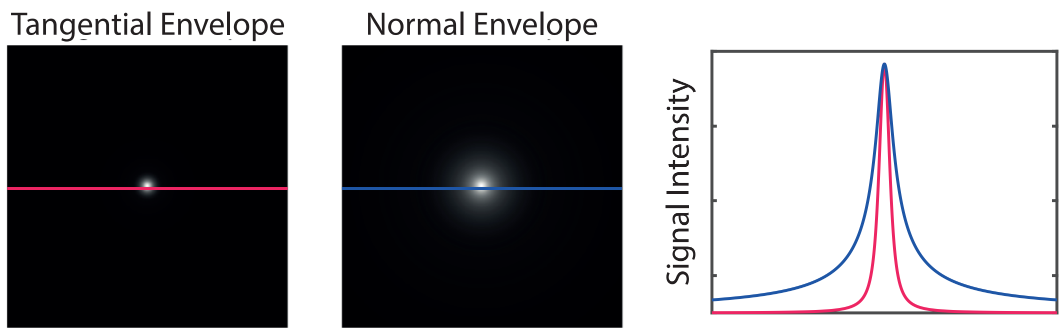

Figure 2.2: Tangential (Red) and normal (Blue) envelopes and 1D cross sections of the envelopes.

Here, $\hat{\mathbf{e}_1}$, $\hat{\mathbf{e}_2}$, and $\hat{\mathbf{e}_3}$ are the unit vectors, where $\hat{\mathbf{e}_1}$ is the one parallel with the velocity vector of the FFP. If $\dot{\mathbf{x}}_s$ is aligned with the x-axis, the collinear and transverse components of the PSF can be written as follows [18]:

$$h_{\|}(x,y,z) = \dot{\mathcal{L}}\left(\frac{H(x,y,z)}{H_{sat}}\right)\frac{G_{zz}^3 z^2}{H(x,y,z)^2} + \frac{\mathcal{L}\left(\frac{H(x,y,z)}{H_{sat}}\right)}{\frac{H(x,y,z)}{H_{sat}}} G_{zz}\left(1 - \frac{G_{zz}^2 z^2}{H(x,y,z)^2}\right) \tag{2.23}$$

$$h_{\perp}(x,y,z) = \dot{\mathcal{L}}\left(\frac{H(x,y,z)}{H_{sat}}\right)\frac{G_{xx}G_{zz}^2 xz}{H(x,y,z)^2} - \frac{\mathcal{L}\left(\frac{H(x,y,z)}{H_{sat}}\right)}{\frac{H(x,y,z)}{H_{sat}}} \frac{G_{xx}G_{zz}^2 xz}{H(x,y,z)^2} \tag{2.24}$$

where $H(x,y,z) = \sqrt{(G_{xx}x)^2 + (G_{yy}y)^2 + (G_{zz}z)^2}$. The collinear and transverse PSF are visualized in Figure 2.3.

In order to scan a FOV, different FFP trajectories are proposed and tested [22]. For the simulations this thesis, the Lissajous trajectory is used, since it is the most commonly used trajectory for FFP MPI scanners[22]. By applying sinusoidal waves with different frequencies through orthogonal drive field coils, a Lissajous trajectory can be achieved. Depending on the ratios of the frequencies applied, the coverage density for a given FOV will be different, as shown in Figure 2.4.

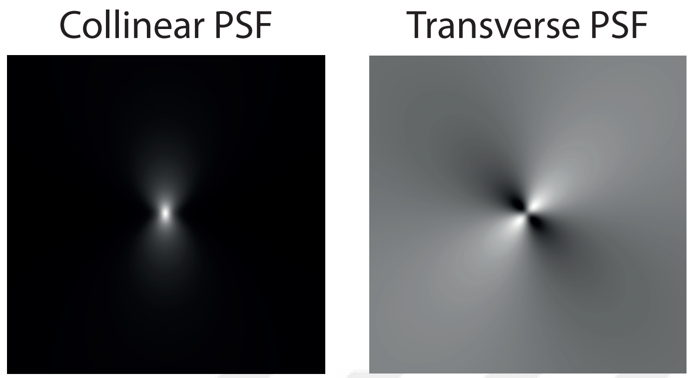

Figure 2.3: Collinear and transverse components of the PSF.

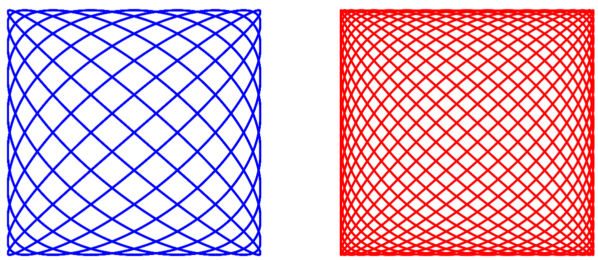

Figure 2.4: The lissajous trajectory with different frequency ratios on the two drive channels, resulting in different coverage densities for a given FOV.

2.2 Image Reconstruction in MPI

There are two methods for reconstructing MPI images. They are system function reconstruction (SFR) approach and x-space reconstruction.

2.2.1 System Function Reconstruction

The received signal u is a linear function of the MNP distribution c, which can be written as

$$f(c) = u \tag{2.25}$$

where f is called the system function. Here, f changes for different scanners, scanning parameters, and MNP type. With the linearity assumption in SFR, the received signal from the combination of distribution c_1 and distribution c_2 is expressed as the summation of the received signal for each distribution separately:

$$f(c_1) = u_1 \tag{2.26}$$

$$f(c_2) = u_2 \tag{2.27}$$

$$f(c_1 + c_2) = u_1 + u_2 \tag{2.28}$$

In the SFR approach, the scanning volume is divided into a grid. Then, c is quantized from a continuous distribution to a vector and the system function f is approximated as a matrix $\mathbf{S}$ called the system matrix. Equation 2.25 can then be transformed to:

$$\mathbf{Sc} = \mathbf{u} \tag{2.29}$$

In order to characterize the system, a point-like MNP distribution is positioned on a grid point such that only one element of $\mathbf{c}$ will be non-zero. The received signal will then correspond to one of the columns of $\mathbf{S}$. Then, this process is repeated for each grid point to acquire the complete system matrix. This characterization process is called calibration. These calibration measurements can take several days depending of how fine the grid is and the size of the scanning volume [14, 23].

After calibration measurements, an unknown MNP distribution $\mathbf{c}_{new}$ can be scanned. Using the received signal $\mathbf{u}_{new}$, the linear equation in Eq. 2.30 needs to be solved in order to find the MNP distribution.

$$\mathbf{Sc}_{new} = \mathbf{u}_{new} \tag{2.30}$$

In reality, due to the non-idealities in hardware, relaxation effects, and magnetic fields MPI systems are not shift invariant. Furthermore, in an actual scan, the entire signal induced on the receive coil is not available due to the direct feedthrough from the excitation coil.

After forming Equation 2.30, the MPI image is reconstructed by finding the solution to the following least squares problem.

$$\underset{\mathbf{c}}{\operatorname{argmin}} \, ||\mathbf{Sc}_{new} - \mathbf{u}_{new}||_2^2 \tag{2.31}$$

In order to solve this problem various direct or iterative inverse solvers are employed. Algebraic Reconstruction Technique (ART) is the most commonly used one in MPI [15, 14].

Algebraic Reconstruction Technique

ART is a solver commonly used in medical imaging due to its fast convergence [15, 14]. In ART reconstruction, the following minimization problem is solved to find the solution to the linear equation:

$$\underset{\mathbf{c}}{\operatorname{argmin}} \, ||\mathbf{Sc} - \mathbf{u}||_2^2 \tag{2.32}$$

where $\mathbf{S}$ is the system matrix, $\mathbf{u}$ is the measurement vector, $\mathbf{c}$ is the unknown MNP distribution to be reconstructed.

ART is an iterative solver. It starts with an initial solution, generally a vector of zeros. In each iteration, the current solution is projected onto one of the rows of the system matrix. This projection is formulated as:

$$c^{l+1} = c^l + \frac{u_j - s_j^* c^l}{||s_j||_2^2} s_j^* \tag{2.33}$$

where c^l is the solution after the l^{th} projection. u_j is the j^{th} element of u. s_j is the j^{th} row of $\mathbf{S}$. There are different ways to chose j for each sub iteration l. The easiest way is choosing rows in order. Another alternative is to select the rows randomly, which can be beneficial for faster convergence [24].

Regularized Weighted Least-Squares

SFR seeks the solution to an ill-posed inverse problem. Therefore, using least-squares as the problem definition does not generate a stable solution. To address this problem, Regularized Weighted Least-Squares problem is considered for the reconstruction, where Tikhonov regularization and weightings according to the row energies of $\mathbf{S}$ are employed. The reconstructed image is then expressed as the solution to the following optimization problem:

$$\underset{\mathbf{c}}{\operatorname{argmin}}\, ||\mathbf{W}^{\frac{1}{2}}\mathbf{S}\mathbf{c} - \mathbf{W}^{\frac{1}{2}}\mathbf{u}||_2^2 + \lambda||\mathbf{c}||_2^2 \tag{2.34}$$

Here, λ is the Tikhonov regluarization parameter, and $\mathbf{W}$ is the following diagonal matrix:

$$\mathbf{W} = diag\Big(\Big(\frac{1}{w_j^2}\Big)_{j=1}^{M}\Big) \tag{2.35}$$

Here, M is the number of frequency components in $\mathbf{S}$ and w_j^2 is the energy of the j^{th} row of $\mathbf{S}$.

The solution to this optimization problem can be achieved using ART via the following extended system [25]:

$$\begin{bmatrix} \mathbf{W}^{\frac{1}{2}}\mathbf{S} & \lambda^{\frac{1}{2}}\mathbf{I} \end{bmatrix} \begin{bmatrix} \mathbf{c} \\ \mathbf{v} \end{bmatrix} = \mathbf{W}^{\frac{1}{2}}\mathbf{u} \tag{2.36}$$

where

$$\mathbf{v} = -\lambda^{\frac{1}{2}}\mathbf{W}^{\frac{1}{2}}\big(\mathbf{S}\mathbf{c} - \mathbf{u}\big). \tag{2.37}$$

2.2.2 X-Space Reconstruction

In x-space reconstruction, there is no need for system calibration. The received signal is velocity compensated and assigned to the instantaneous location of the FFP [17, 18]. X-space reconstruction can be expressed as follows:

$$\mathrm{IMG}(x_s(t)) = \frac{s(t)}{B_1 m G \dot{(x)}_s(t)/H_{sat}} = c(x) * \dot{\mathcal{L}}[Gx/H_{sat}]|_{x=x_s(t)} \tag{2.38}$$

Although this approach does not need a calibration scan, the reconstructed image is blurred by $\dot{\mathcal{L}}[Gx/H_{sat}]$, which is the PSF of the imaging system.

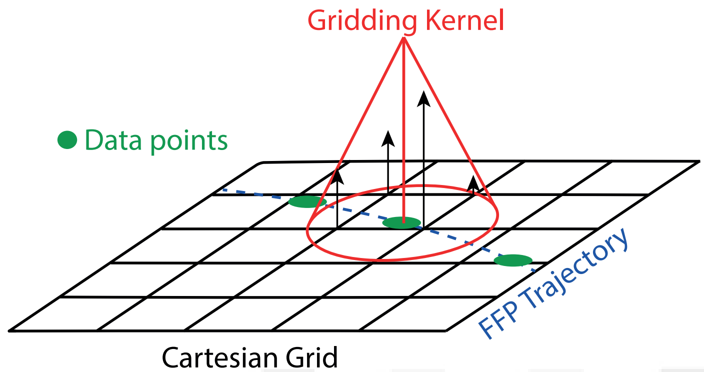

Figure 2.5: Data points on FFP trajectory are convolved with the gridding kernel and re-sampled onto a Cartesian grid.

In MPI, when non-Cartesian FFP trajectories are employed, IMG needs to be gridded to a Cartesian grid before it can be displayed. The gridding algorithm explained in Figure 2.5 can be used for MPI [21]:

$$\mathrm{IMG}_{\mathrm{gridded}}(x) = \sum_{i=1}^{N_s} \frac{(\mathrm{IMG}(x_s(t_i)) * k(x))\text{Ш}(\frac{x}{\Delta x})}{(s(x) * k(x))\text{Ш}(\frac{x}{\Delta x})} \tag{2.39}$$

where,

$$s(x) = \sum_{i=1}^{N_s} \delta\left(x - x_i\right) \tag{2.40}$$

$$\tag{2.41}$$

Here, $s(x)$ is a non-Cartesian sampling function composed of impulses at sampled FFP locations, $k(x)$ is the gridding kernel, Ш is the comb function used for re-sampling onto the Cartesian grid, Δx is the spatial distance between grid points on the Cartesian grid, and N_s is the total number of acquired samples.

For the gridding kernel, a Kaiser-Bessel window can be used:

$$k(\mathbf{x}) = I_0\left(\beta\sqrt{1 - \left(\frac{2\,\|\mathbf{x}\|}{w_k \Delta x}\right)^2}\right) \tag{2.42}$$

where,

$$\Delta x = \frac{x_{FOV}}{N} \tag{2.43}$$

Here, I_0 is the zero-order modified Bessel function of the first kind, x_{FOV} is the extent of the FOV, N is the reconstructed image size, w_k is the full kernel width in grid units, and β is the shape parameter of the Kaiser-Bessel kernel. The choice of parameters for gridding algorithm are beyond the scope of this thesis and are explained in detail in [21].

Chapter 3

Parameter Robustness Analysis for SFR

This chapter is based on the publication titled "Parameter Robustness Analysis for System Function Reconstruction", Abdullah Ömer Arol, Ali Alper Ozalsan, Emine Ulku Saritas, Proceedings of the 10$^{\text{th}}$ International Workshop on Magnetic Particle Imaging (IWMPI), 2020.

3.1 Introduction

SFR is one of the main image reconstruction methods for MPI [1, 20]. In SFR, the system matrix (SM) characterizes the mapping between the received MPI signal and MNP distribution at each position in the FOV. However, SM is specific to scanner and trajectory parameters, as well as the physical parameters of MNP. A change in any one of these parameters requires a new calibration scan, which can be time consuming.

In this chapter, the parameter robustness of SFR is analyzed. With simulations, the effects of using an existing SM (i.e., without performing a new calibration) in the case of a change in one of the scanning parameters are investigated. The aim of this analysis is to determine the extent of change in parameters that SFR can withstand without a new calibration.

3.2 Material and Methods

MATLAB simulations were performed using an in-house MPI simulation toolbox to investigate the effects of using mismatched parameters during calibration and imaging. First, calibration scans on a 40×40 grid for an MPI system with 2cm×2cm FOV were simulated. Simulations were repeated with ideal and non-ideal selection fields with gradients $(3, 3, -6)T/m/\mu_0$ along (x,y,z) directions as shown in Figure 3.1. Single-core monodisperse MNP with 25-nm diameter was assumed. A Lissajous trajectory in x-y plane was created using the following 2D drive field (DF):

$$H_x = H_p \sin(2\pi f_0 t) \tag{3.1}$$

$$H_y = H_p \sin(2\pi f_1 t) \tag{3.2}$$

Here, $f_0 = 25kHz$ and $f_1 = 24.75kHz$ was utilized, with $H_p = 30mT/\mu_0$ to cover the desired FOV.

SFR seeks the solution to an ill-posed inverse problem. Therefore, as explained in Chapter 2, regularization is required to achive a stable reconstruction. For reconstructions in this chapter, regularized weighted least-squares problem was considered. Tikhonov regularization and weightings according to the row energies of SM were employed as suggested in [15]. Accordingly, the rows of SM with energies less than 4% of the energy of the row with the maximum energy were removed. In addition, the frequencies up to $1.5 \times f_0$ (i.e., the fundamental frequency bands) were also filtered out. The reconstructed image was expressed as the solution to the optimization problem in Equation 2.34. This problem was solved using ART and the regularization parameter chosen for each case separately. For quantitative image quality comparison, the reconstructed images were compared with the phantom using the Peak Signal-to-Noise Ratio (PSNR) metric [26].

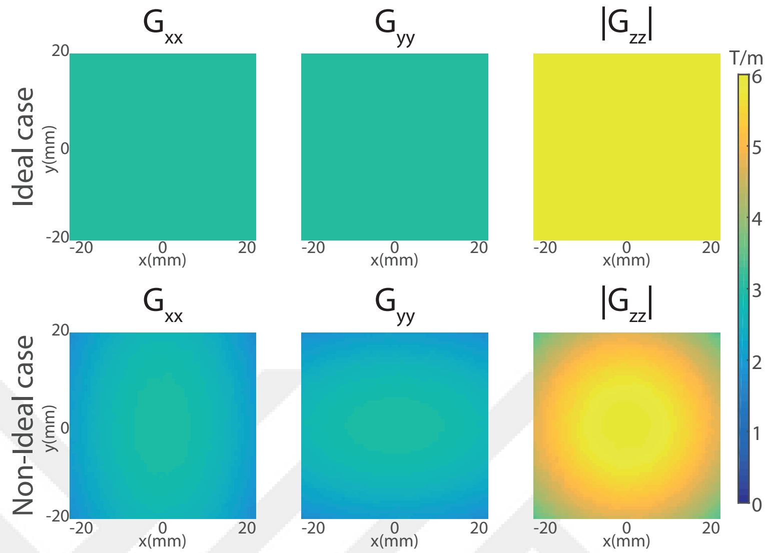

Figure 3.1: Selection field gradients for the ideal and the non-ideal case at the imaging plane of MPI scanner. In the non-ideal case, the gradients of the selection field are position dependent.

After obtaining the SM, the following changes were considered to evaluate the parameter robustness of SFR.

3.2.1 Change in MNP Diameter

The ideal MNP magnetization curve is modeled by the Langevin function [17], which is a strong function of the MNP diameter. In day-to-day usage of an MPI scanner, there may be a need to change the MNP type, e.g., due to availability of a better MNP or for testing the performance of a new MNP. Here, the MNPs were assumed to be single-core and monodisperse, and the diameter was varied between 10-35 nm. Relaxation effects were ignored.

3.2.2 Change in FOV Size

During imaging, one may want to change the FOV size to cover a wider region than initially foreseen, or to zoom into a region of interest. Here, FOV size was varied by changing the DF amplitude, H_p. As exemplified in Fig. 3.2, the FOV covered was varied between 40% and 200% of the original FOV for which the SM was acquired.

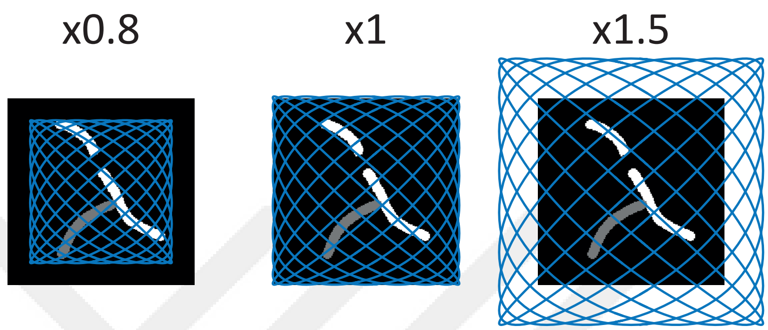

Figure 3.2: Effect of changing drive field amplitude on the covered FOV.

3.2.3 Change in Trajectory Density

The frequency ratio of the two DFs in Eq. 3.1 determines the trajectory density, N_p, as follows:

$$f_0 = \frac{N_p}{N_p - 1} f_1. \tag{3.3}$$

As exemplified in Fig. 3.3, depending on the ratios of DF frequencies, both the duration of the trajectory ($T_R = N_p/f_0$) and the distances between sampled points change. Hence, N_p affects the reconstructed image considerably. Previous work on trajectory analysis has shown that higher N_p yields higher resolution MPI images for both SFR and x-space reconstructions [22, 21]. Therefore, during imaging, one may want to increase N_p to achieve a higher quality image. Change in the hardware that generates the DFs can also affect the frequency ratios between f_0 and f_1. Very small shifts in the ratio of DF frequencies can lead to drastic changes in the scanning trajectory.

Here, N_p was varied while keeping f_0 fixed. Note that this change requires the frequency of the second coil (i.e., f_1) to change. However, the change in frequency is relatively small and can still fall within the resonant band for the impedance matching of that coil.

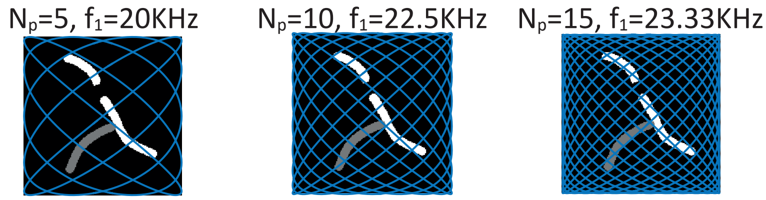

Figure 3.3: Sample trajectories with small N_p values for illustration purposes. Much denser trajectories were used in actual simulations. Here, f_0 was kept constant at 25kHz.

3.3 Results and Discussion

The results of using an existing SM in the case of a change in one of the three parameters listed above are shown below.

3.3.1 Effect of Changing MNP Diameter

Figure 3.4 shows the results of utilizing a MNP with a diameter different than the one in the calibration scan. When a larger MNP is utilized, the performance of SFR does not change visibly, whereas using a smaller MNP reduces the image quality considerably. PSNR values for the images in Figure 3.4 are shown in Figure 3.5. These results imply that the reconstructions from a better MNP are restricted by the quality of the existing SM, whereas reconstructions from a lower quality MNP are restricted by the performance of the MNP itself.

A change in MNP diameter changes the effective size of the FFP, as well as the ratios between the signals at higher harmonics. Here, a new and relatively simple method of correction for reconstruction with a different MNP diameter is proposed to compensate for the change in higher harmonics ratios. Accordingly, a point source containing the new MNP was placed at the origin, and a calibration scan was acquired for this point only. The existing SM at all other positions were then corrected to match the higher harmonic ratio of this one-point calibration. As shown in Figure 3.4 and 3.5, a considerable improvement in image quality is achieved for 10-nm and 15-nm diameter cases. According to the PSNR metric,

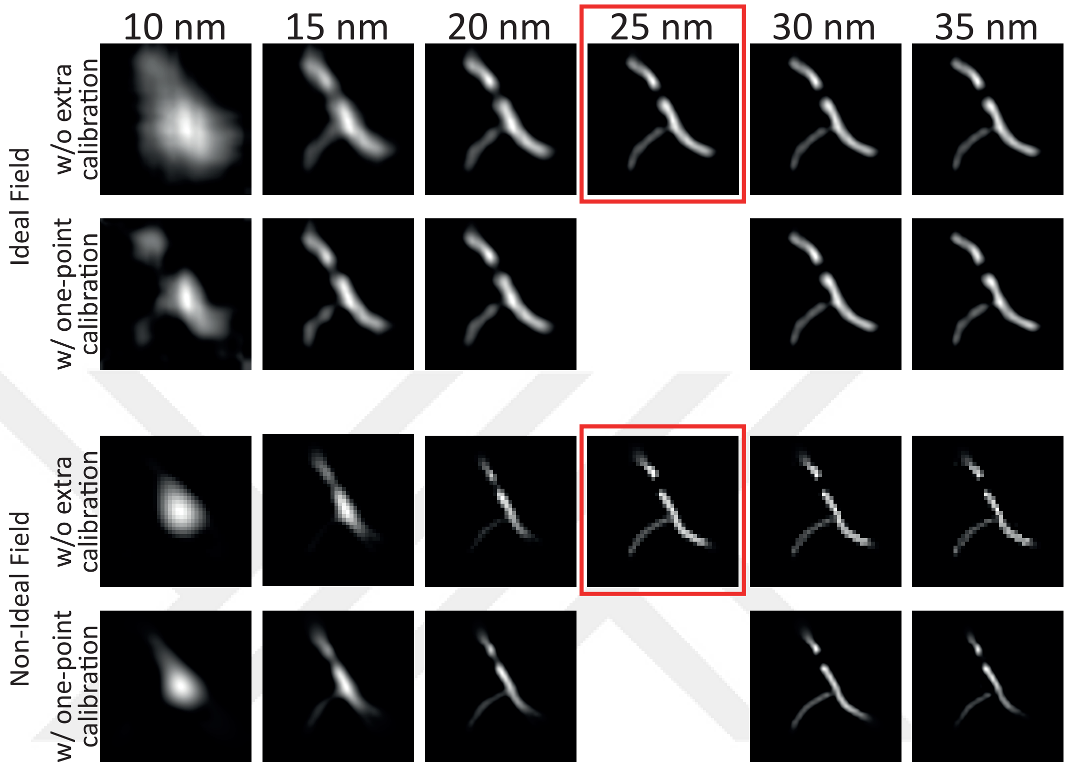

Figure 3.4: First and third rows: Reconstructed images for different sizes of particles using an SM acquired for 25 nm. Second and fourth rows: Improvements achieved with one-point measurement correction to the SM.

for the ideal field case, the image quality improves by 3.17 dB and 1.38 dB for the 10-nm and 15-nm diameter cases, respectively. For the non-ideal field case, the improvements are 0.97 dB and 0.27 dB, respectively. A similar analysis and correction may be utilized when incorporating nanoparticle relaxation effects.

3.3.2 Effect of Changing FOV Size

As shown in Figure 3.6, no severe artifacts were seen in the reconstructed images for different FOV sizes. However, for bigger FOVs, the effective size of a pixel gets larger, causing a loss of resolution in the image. This in turn reduces the PSNR value of the reconstructed image, as shown in Figure 3.7. Accordingly, the PSNR at FOV scale 2 is 3.63 dB lower than that at FOV scale 1 for the ideal field case. For the non-ideal field case, the PSNR at FOV scale 2 is 0.98 dB lower

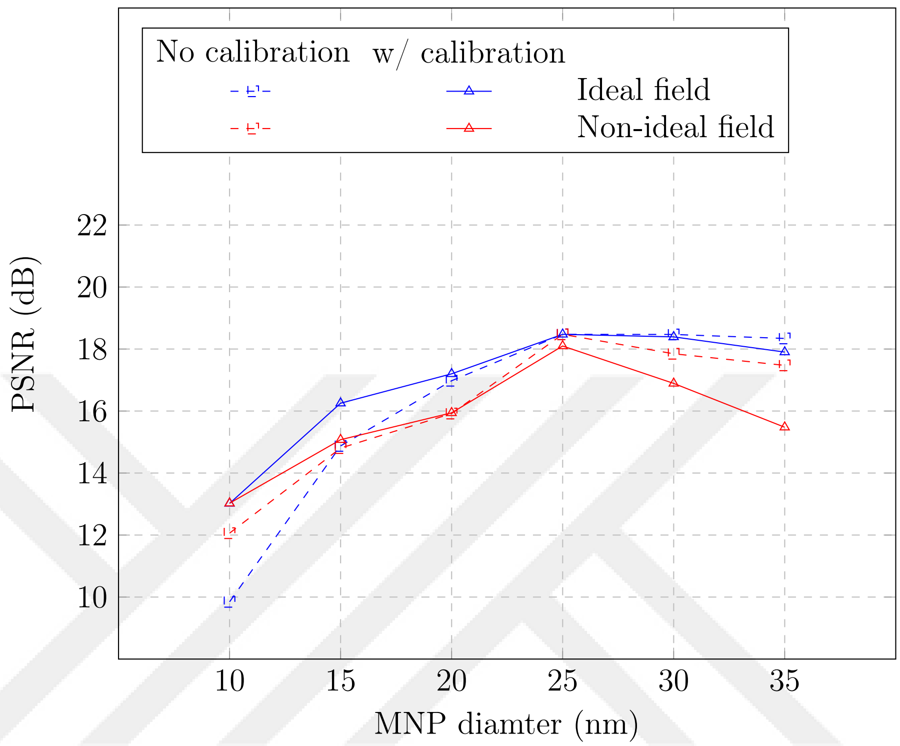

Figure 3.5: PSNR values of the reconstructed images for different sizes of MNPs.

than that at FOV scale 1.

3.3.3 Effect of Changing Trajectory Density

Changing N_p changes the relative timing of the trajectory, where the same point in the FOV is traversed at a different time point. As shown in Figure 3.8, larger changes in N_p causes a warping/remapping effect in the reconstructed image, as different portions of the MNP distribution is mapped to incorrect locations. This warping and remapping effects results in significant PNSR drop as shown in Figure 3.9 even for 10% change in N_p value which corresponds to 0.53% shift in f_1. For a 10% change in N_p, the PSNR drops by 3.79 dB for the ideal field case, whereas it drops by 3.82 dB for the non-ideal field case. These results demonstrate that SFR is very sensitive to the ratio between the drive field frequencies.

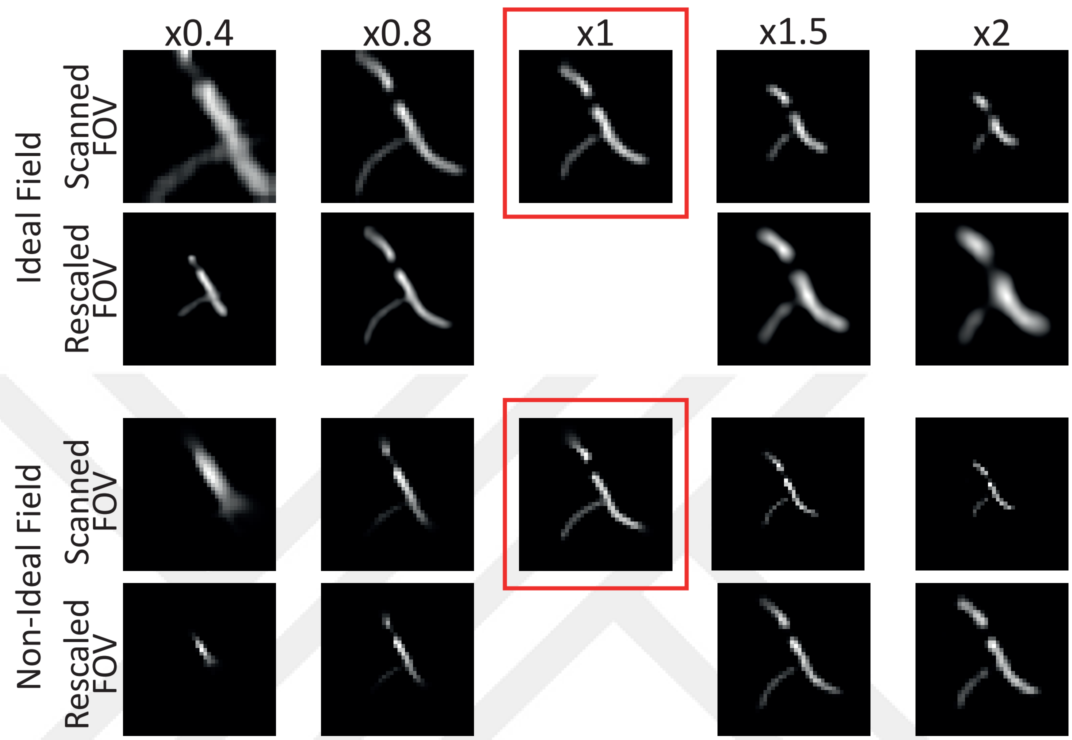

Figure 3.6: Reconstructed images for different FOV sizes for the ideal and non-ideal cases. The second and forth row show the rescaled images to the correct FOV sizes. The effective size of a pixel gets bigger, causing a loss of resolution for larger FOVs. In addition, non-ideal magnetic fields create artifacts at the edges of smaller FOV sizes.

3.4 Conclusions

In this chapter, the effects of scanning parameter changes on the reconstructed images for SFR were analyzed. The results show that small changes on scanning and nanoparticle parameters do not require new calibration scans, as they yield comparable image quality. It is also shown that the quality of reconstructions can be improved by using a one-point calibration scan when a different MNP is utilized during imaging when compared to the one used in the calibration.

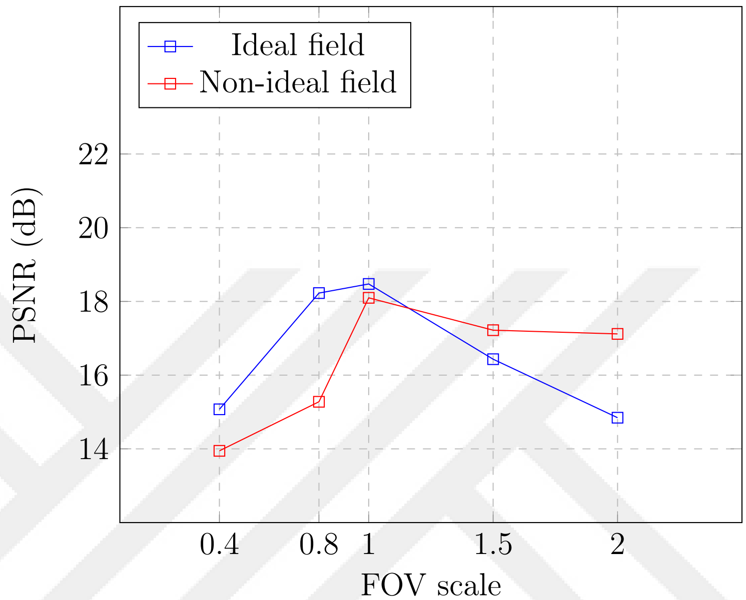

Figure 3.7: PSNR values for different FOV sizes.

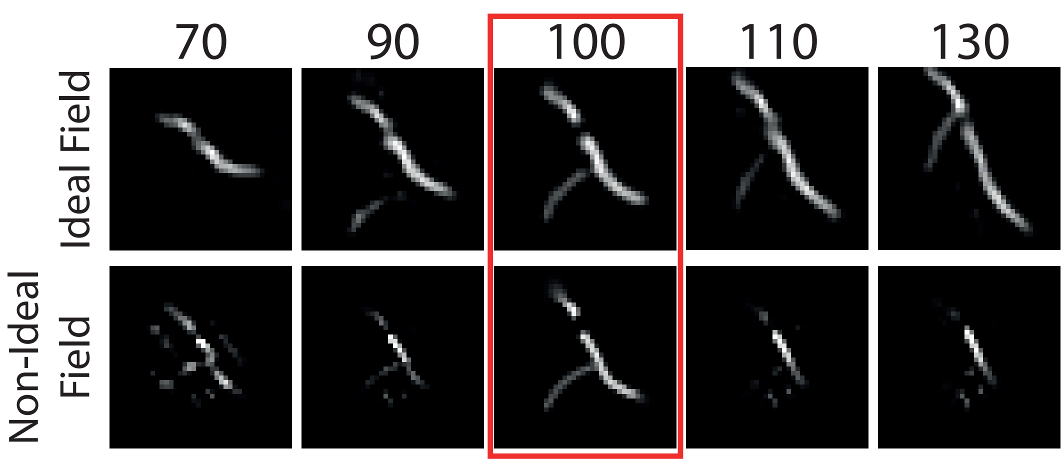

Figure 3.8: Resulting images for different N_p values for ideal and non-ideal magnetic fields.

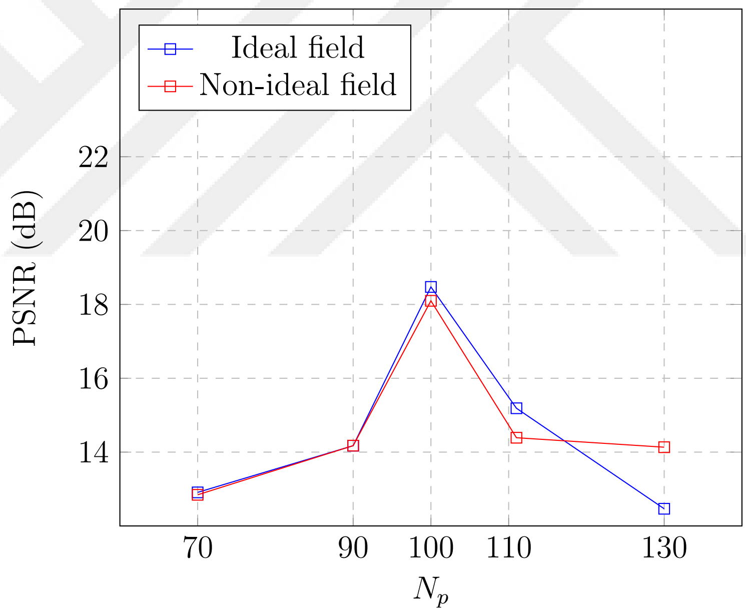

Figure 3.9: PSNR values for different N_p values.

Chapter 4

A Deblurring Network for Magnetic Particle Imaging

This chapter is based on the publication titled "A Super-Resolution Network for MPI", Abdullah Ömer Arol, Ali Alper Ozalsan, Semih Kurt, Tolga Çukur, Emine Ulku Saritas, Proceedings of the 9$^{\text{th}}$ International Workshop on Magnetic Particle Imaging (IWMPI), 2019.

4.1 Introduction

As explained in Section 2.2, there are two main approaches for image reconstruction in MPI. Both reconstruction techniques have their advantages and limitations. The main limitation of SFR is the extensive duration of the calibration scan. Depending on the desired resolution and scanning volume, the calibration process can take close to 24 hours [20, 27]. Although there are some procedures for reducing the calibration time [28, 29], the calibration scan needs to be repeated every time a scan parameter is changed. In order to change the FOV size, voxel size or the location of the FOV in the scanner, a new calibration scan is needed. Using a new type of MNP also requires a new calibration scan.

The alternative image reconstruction approach, x-space reconstruction, does not require any calibration measurements. However, it produces blurry images because of the convolution of MNP distribution with a PSF, as given in Eq. 2.17. This blurring reduces the quality of the reconstructed image.

In this thesis, a deblurring network for MPI is introduced to improve image quality in x-space reconstruction. This method is inspired by the success of machine learning methods in various computer vision problems [30, 31, 32, 33, 34, 35]. The proposed network learns an end-to-end mapping between the blurred x-space gridded MPI images and MNP distributions.

4.2 Methods

4.2.1 Neural Network Architectures

Deblurring is a classical problem in computer vision that aims to remove the blurring effect from an image. Due to convolution with PSF, information at high spatial frequencies will be lost permanently, creating a lack of information to fully recover the original image. Therefore, deblurring is an ill-posed problem with infinitely many solutions. To overcome this problem, many learning-based approaches have been developed, utilizing machine learning algorithms to capture the relation between the blurred image and the underlying original image based on training data. Here, first two blurry images are reconstructed from the computed virtual collinear coil and transverse coil signals using an x-space-based automated gridding algorithm [21]. Then, the deblurring network takes both of the gridded collinear and transverse MPI images as inputs and reduces blurring to more accurately estimate the MNP distribution.

In this thesis, two different neural network architectures are proposed for this problem.

Convolutional Neural Network

The convolutional neural network (CNN) architecture in this thesis is adopted from a single-image super resolution (SR) network presented in [31]. SR is a classical problem in computer vision that aims to recover a high-resolution image from its low-resolution counterpart. In this thesis, the network takes x-space gridded collinear and transverse MPI image as inputs and reduces blurring to more accurately estimate the MNP distribution.

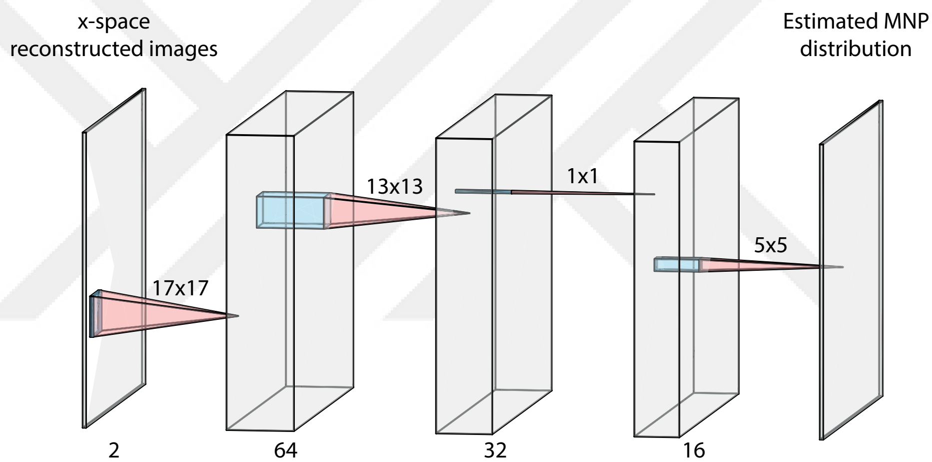

Figure 4.1: CNN architecture.

Four convolutional layers were used and rectified linear units were employed between hidden layers as activation functions. The number and sizes of filters are shown in Figure 4.1.

Generative Adversarial Networks

The generative adversarial network (GAN) architecture in this thesis is adopted from an image-to-image translation network presented in [36]. Image-to-image translation networks aim to learn how to transform images from one domain to another. Here, the network is trained to learn translating x-space gridded collinear and transverse MPI images to MNP distribution. In this work, the hyperparameters of the network were adopted from [36]. The model architecture is shown in Figure 4.2

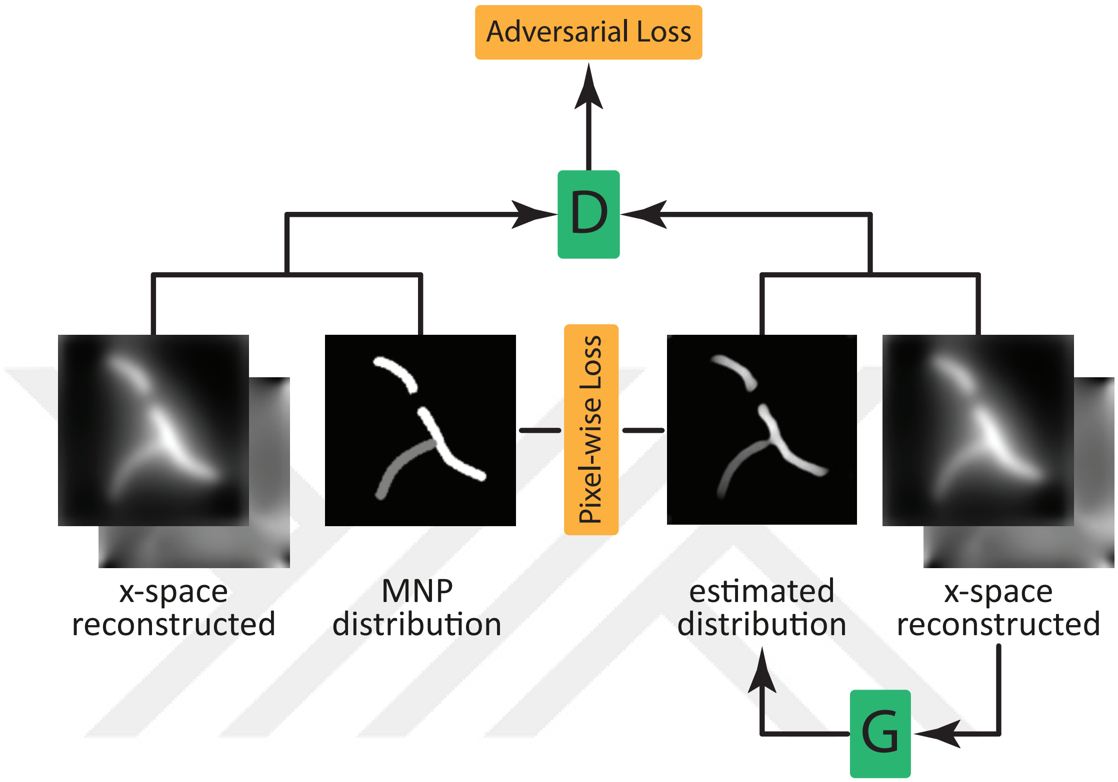

Figure 4.2: GAN architecture.

4.2.2 Numerical Experiments

To evaluate the proposed networks, simulations were performed using an in-house MPI simulation toolbox based on an MPI system with 2cm×2cm FOV. MNPs with 25 nm dimater were placed on a 280×280 grid in this FOV. Selection field gradients of (3,3,-6) T/m/μ_0 were assumed along (x,y,z) directions. For scanning the FOV, a Lissajous trajectory with drive field frequencies 24.75 kHz and 25 kHz along x- and y- directions was used. These frequencies correspond to a trajectory density of $N_p = 100$. The images were reconstructed using an x-space-based gridding algorithm that automatically tunes the reconstruction parameters from the scanning trajectory [21]. This gridding algorithm takes in the MPI signals from two receive coils oriented along x- and y-directions, and computes the signals for two virtual coils: one that is placed collinear to the FFP velocity vector at all times, and the other placed transverse to it. Accordingly, the gridding algorithm outputs two separate MPI images: collinear image and a transverse image. Due to the collinear PSF being better behaved, the resulting collinear x-space image has considerably higher resolution and image quality than the transverse image.

To train the networks, a dataset of 2800 realistic MPI images were generated. The training dataset was generated using a phantom called a Rotating and Sliding Connected Codded Calibration Scene (RSC-CCS), which was previously proposed for faster calibration measurements for SFR [37]. In RSC-CCS, a single calibration phantom larger than the FOV is rotated and translated, while calibration measurements are acquired. The calibration phantom used in simulations is shown in Figure 4.3. This calibration phantom incorporates important two important modifications compared to the original RSC-CCS idea: It contains sections with different MNP concentrations and different channel thicknesses. These modifications are necessary for the networks to be able to output non-binary images with different channel thicknesses. A sample data pair generated using RSC-CCS is shown in Figure 4.4, showing the collinear and transverse images for a small section of the RSC-CCS phantom.

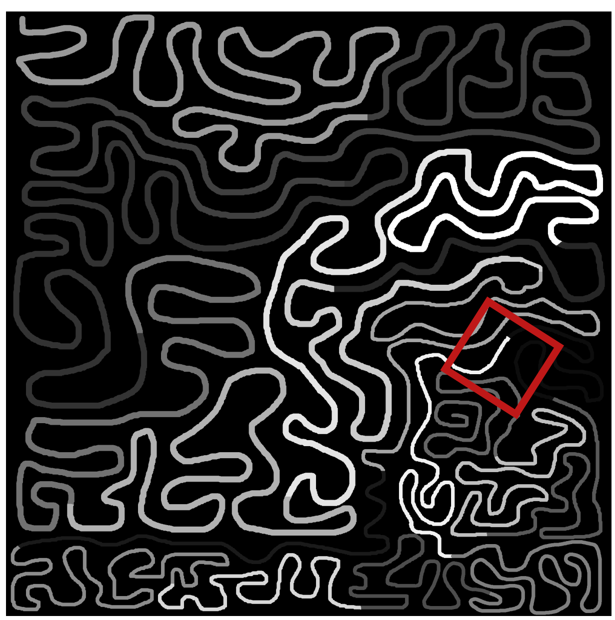

Figure 4.3: RSC-CCS phantom used for dataset generation. The red box is a sample scene used in creating the dataset. The collinear and transverse images corresponding to the boxed region are shown in Figure 4.4.

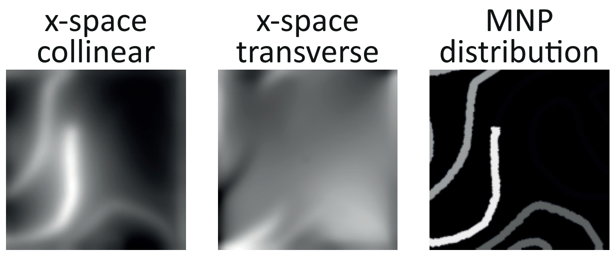

Figure 4.4: A part of RSC-CCS phantom and gridded collinear and transverse images.

4.3 Results and Discussion

The proposed neural networks were tested with the phantom shown in Figure 4.5. The MPI signals for the phantom for different scanning parameters were simulated and reconstructed with automated x-space gridding reconstruction. Different MNP diameters, FOV sizes, and trajectory densities were simulated for the given phantom to analyze the robustness of the proposed networks.

For quantitative image quality comparison, the PSNR values for the reconstructed images were compared with the results of SFR from Chapter 3. However, in Chapter 3, SM was gathered for 2cmx2cm FOV gridded into 40x40 pixels, where it takes 1600 calibration measurements to fully sample the SM. In this chapter, neural networks in proposed methods were trained for the same FOV gridded into 280x280 pixels. In this case, a fully sampled SM would require 78,400 calibration measurements. Here, only 2800 calibration measurements were utilized from different positionings of the RSC-CCS phantom, corresponding to an accelaration factor of 28 when compared to the fully sampled SM case.

4.3.1 Change in MNP Diameter

The MNP magnetization is modeled by the Langevin function as described in Chapter 2. The PSF of the system depends on the MNP diameter. As the MNP size gets smaller, the PSF gets wider and the x-space reconstructed image becomes more blurry. The effect of this blur can be seen in Figure 4.6. MNPs

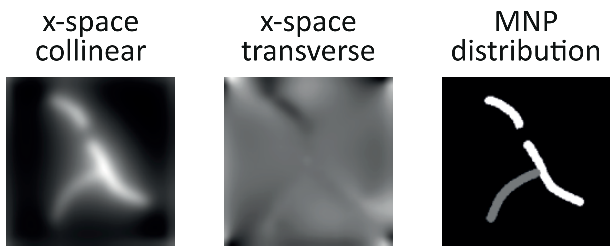

Figure 4.5: Test phantom and the corresponding collinear and transverse images, which are the inputs to the neural networks. The collinear and transverse images correspond the case where the MNP diameter is 25 nm, FOV is 2cmx2cm (i.e., FOV scale = 1), and $N_p = 100$.

with a diameter of 25 nm were used for creating the training dataset with the RSC-CCS phantom shown in Figure 4.3. Both CNN and GAN can successfully handle larger MNP diameters, as the image quality remains comparable to the original case. The networks can also handle slightly smaller MNP sizes than in the training. As the MNP diameter is further reduced to 15 nm or lower, the image quality is degraded considerably for both networks. PSNR values for the reconstructed images for both neural networks when compared to SFR are show in Figure 4.7. GAN provides the highest image quality among the tested reconstruction methods. It provides 2.36 ± 0.73 dB improvement over SFR, 1.65 ± 1.12 dB improvement over SFR with one-point calibration, and 1.47 ± 1.04 dB improvement over CNN across all the tested diameters. Both GAN and CNN provide better image quality than SFR for all MNP diameters. While SFR with one-point calibration improves the reconstruction quality for smaller MNP diameters, both of the proposed networks provide better image quality at higher MNP diameters.

4.3.2 Change in FOV Size

In SFR, the number of pixels in the reconstructed image is fixed by the number of columns of the system matrix. Therefore, increasing the FOV size in SFR creates an inherent loss of resolution. However, in x-space reconstruction, the resulting pixel size can be changed depending on the size of the FOV during

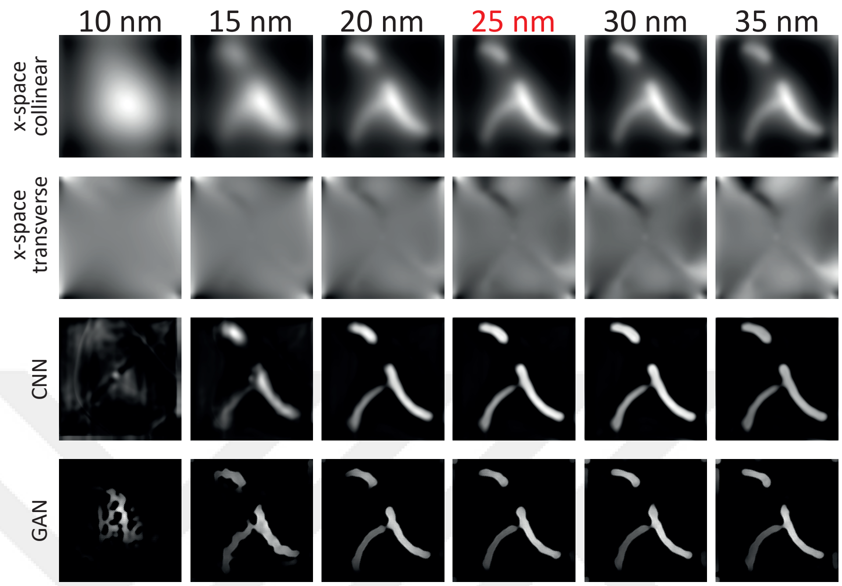

Figure 4.6: Reconstructed images for different MNP diameters. 25 nm is the MNP diameter used in the training dataset.

image reconstruction. This is advantageous for the proposed approach as the blurring effect remains constant as the FOV changes. As a result, changing the FOV size does not create any severe artifacts in the network results, as shown in Figure 4.8. As shown in Figure 4.9, the reconstruction quality for GAN is the highest among the tested methods. It provides 2.98 ± 1.17 dB improvement over SFR and 2.12 ± 1.46 dB improvement over CNN across all the tested FOV scales. The reconstruction quality for CNN is also higher than that of SFR at all tested FOV scales, except at the smallest FOV scale of 0.4.

4.3.3 Change in Trajectory Density

The blurring levels of reconstructed images for different trajectory densities do not change significantly in x-space reconstruction. Therefore, changing the trajectory density does not affect the quality of the network results. As shown in Figure 4.10, there is no visible artifacts in the resulting images for different N_p values. PSNR values for the resulting images are shown in Figure 4.11. Accordingly, GAN provides 5.76 ± 2.49 dB improvement over SFR and 1.15 ± 0.49 dB improvement

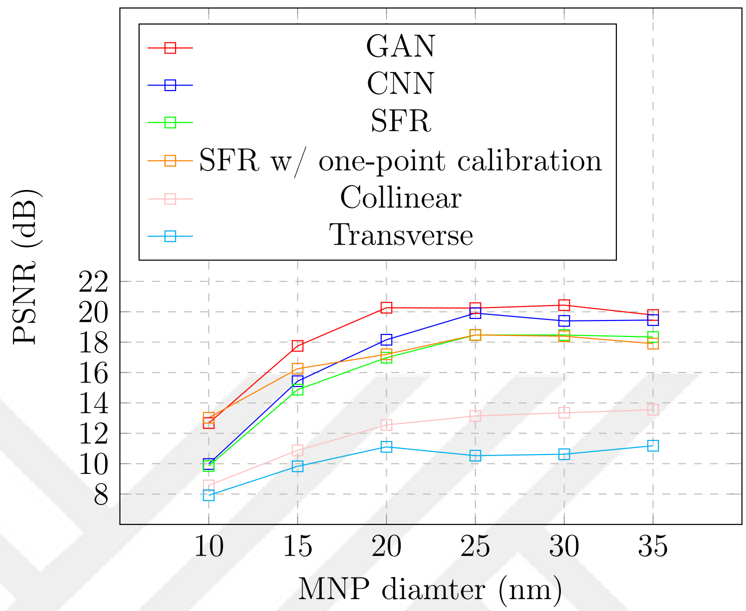

Figure 4.7: PSNR values of reconstructed images for different sizes of MNPs.

over CNN across all the tested N_p values. It is safe to claim that the proposed networks can handle trajectory density changes better than SFR.

4.4 Conclusion

In this chapter, a novel approach using neural networks to reduce the blurring in x-space reconstructed MPI images is proposed. The proposed networks can also handle moderate changes in scanning parameters without the need of an additional training. Among the proposed deblurring networks, GAN provides improved image quality over CNN and SFR for all the tested cases.

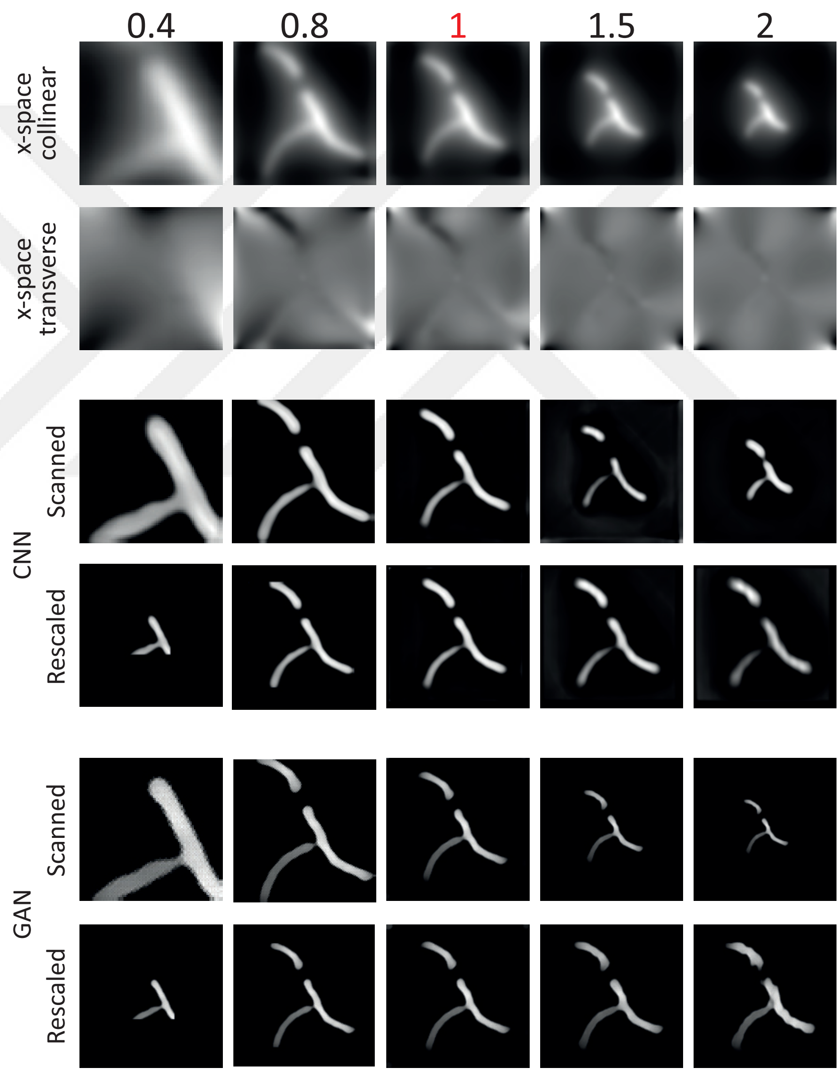

Figure 4.8: Reconstructed images for different size of FOVs.

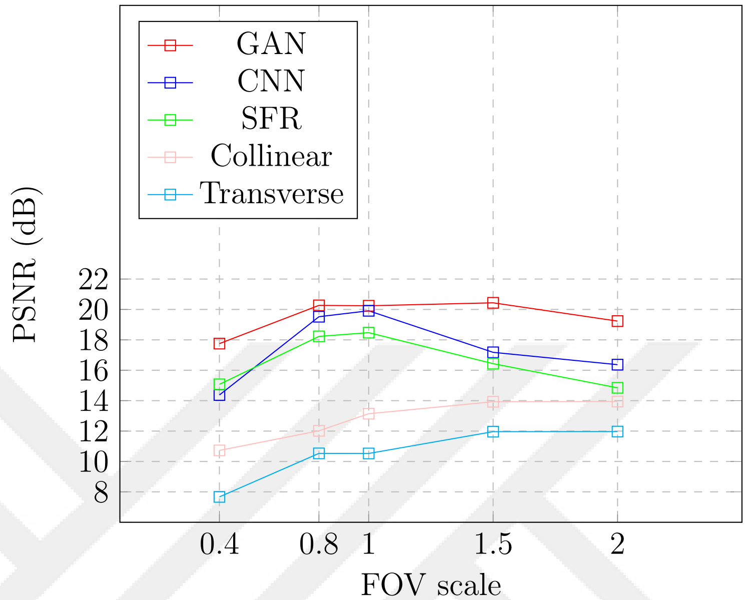

Figure 4.9: PSNR values for different FOV sizes.

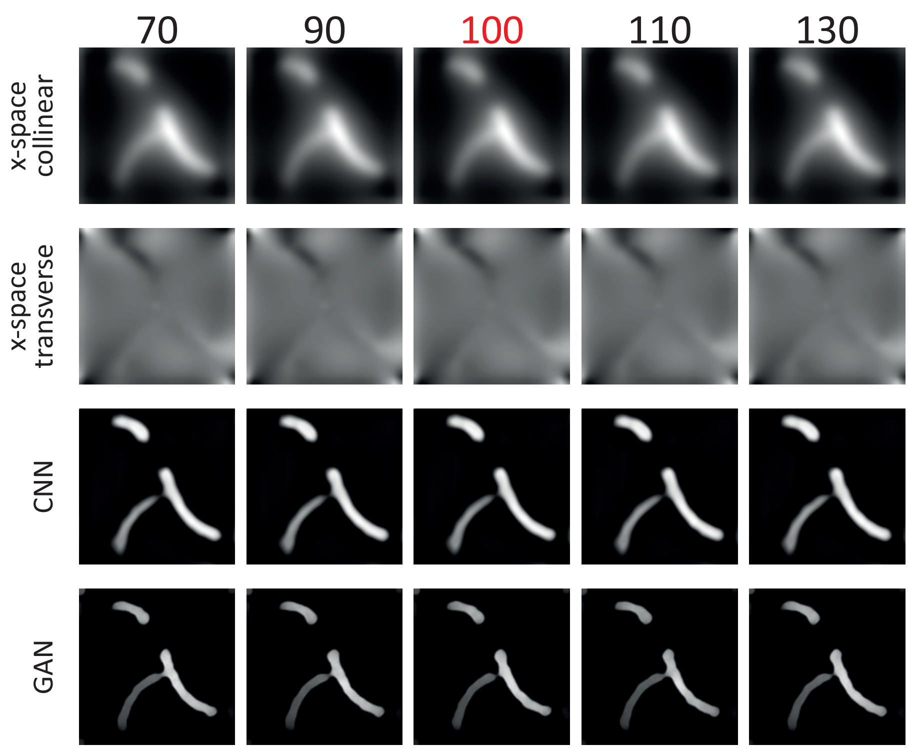

Figure 4.10: Reconstructed images for different trajectory densities. 100 is the trajectory density used in the training dataset.

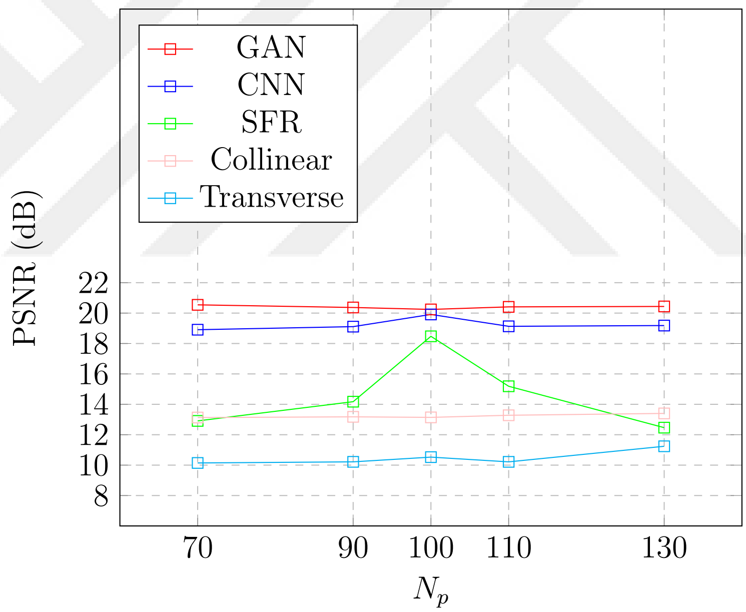

Figure 4.11: PSNR values for different N_p values.

Chapter 5

Conclusion

In this thesis, two different analyses on reconstruction methods in MPI were presented. In Chapter 3, the robustness of SFR against parameter changes at scan time was investigated. It is shown that SFR can handle small changes on the scanning parameters and can yield comparable image quality without requiring a new calibration scan. The quality of reconstructions can be improved by using the proposed one-point calibration method when using MNPs with different diameters. In addition, it is shown that SFR is particularly sensitive to changes in the scanning trajectory density.

In Chapter 4, a new learning-based solution for reducing the blurring in x-space reconstruction was proposed, which requires fewer calibration scans compared to SFR. The proposed solution can also handle different scanning parameters without the need for additional training. The GAN approach, in particular, provides improved image quality over SFR for all the tested cases. Noise analysis of the proposed method was not included here. Depending on the differences between the noise levels for training measurements and test measurements, the reconstruction quality of the proposed algorithm might be affected. Studying the effects of different noise levels at different stages remains an important future work. The relaxation effect of the MNPs was also not taken into consideration in this thesis. The Langevin model for the magnetization response of the MNPs assume that the MNPs can align their magnetization with the applied magnetic field instantaneously. In reality, however, the MNP magnetization response is delayed by the relaxation effects. This in turn causes a blurring and a signal loss in the resulting MPI images. The relaxation effect is also dependent on the environmental properties of the MNPs, such as the temperature and viscosity. Hence, the effects of relaxation on image quality needs to be investigated for a more realistic application of the proposed method.

Bibliography

[1] B Gleich and J Weizenecker. “Tomographic imaging using the nonlinear response of magnetic particles”. In: *Nature* 435.7046 (2005), pp. 1214–1217. ISSN: 1476-4687. DOI: 10.1038/nature03808.

[2] J Weizenecker, J Borgert, and B Gleich. “A simulation study on the resolution and sensitivity of magnetic particle imaging.” In: *Physics in Medicine and Biology* 52.21 (2007), pp. 6363–6374. ISSN: 0031-9155. DOI: 10.1088/0031-9155/52/21/001.

[3] Patrick W Goodwill et al. “An x-space magnetic particle imaging scanner”. In: *Review of Scientific Instruments* 83.3 (2012), p. 033708.

[4] Emine U. Saritas et al. “Magnetic particle imaging (MPI) for NMR and MRI researchers”. In: *Journal of Magnetic Resonance* 229 (2013), pp. 116–126. ISSN: 10907807. DOI: 10.1016/j.jmr.2012.11.029.

[5] Lisa M Bauer et al. “Magnetic particle imaging tracers: state-of-the-art and future directions”. In: *The Journal of Physical Chemistry Letters* 6.13 (2015), pp. 2509–2517.

[6] Julian Haegele et al. “Visualization of instruments for cardiovascular intervention using MPI”. In: *Springer Proceedings in Physics*. Vol. 140. 2012, pp. 211–215. ISBN: 9783642241321. DOI: 10.1007/978-3-642-24133-8_34.

[7] Jurgen Rahmer et al. “Interactive Magnetic Catheter Steering with 3-D Real-Time Feedback Using Multi-Color Magnetic Particle Imaging”. In: *IEEE Transactions on Medical Imaging* 36.7 (2017), pp. 1449–1456. ISSN: 1558254X. DOI: 10.1109/TMI.2017.2679099.

[8] Sarah Vaalma et al. “Magnetic particle imaging (MPI): experimental quantification of vascular stenosis using stationary stenosis phantoms”. In: *PloS one* 12.1 (2017), e0168902.

[9] Johannes Salamon et al. “Magnetic particle / magnetic resonance imaging: In-vitro MPI-guided real time catheter tracking and 4D angioplasty using a road map and blood pool tracer approach”. In: *PLoS ONE* 11.6 (2016), pp. 1–14. ISSN: 19326203. DOI: `10.1371/journal.pone.0156899`.

[10] Anna C Bakenecker et al. “Magnetic particle imaging in vascular medicine”. In: *Innovative Surgical Sciences* 3.3 (2018), pp. 179–192.

[11] Mustafa Utkur, Yavuz Muslu, and Emine Ulku Saritas. “Relaxation-based viscosity mapping for magnetic particle imaging”. In: *Physics in Medicine and Biology* 62.9 (2017), p. 3422.

[12] Yavuz Muslu et al. “Calibration-free relaxation-based multi-color magnetic particle imaging”. In: *IEEE Transactions on Medical Imaging* 37.8 (2018), pp. 1920–1931.

[13] Erica E Mason et al. “Design analysis of an MPI human functional brain scanner”. In: *International Journal on Magnetic Particle Imaging* 3.1 (2017), pp. 1–12.

[14] Jürgen Rahmer et al. “Signal encoding in magnetic particle imaging: Properties of the system function”. In: *BMC Medical Imaging* 9.1 (2009), p. 4. ISSN: 14712342. DOI: `10.1186/1471-2342-9-4`.

[15] T Knopp et al. “Weighted iterative reconstruction for magnetic particle imaging”. In: *Physics in Medicine and Biology* 55.6 (2010), p. 1577.

[16] Jürgen Rahmer et al. “Analysis of a 3-D system function measured for magnetic particle imaging”. In: *IEEE Transactions on Medical Imaging* 31.6 (2012), pp. 1289–1299.

[17] Patrick W Goodwill and Steven M Conolly. “The X-space formulation of the magnetic particle imaging process: 1-D signal, resolution, bandwidth, SNR, SAR, and magnetostimulation”. In: *IEEE Transactions on Medical Imaging* 29.11 (2010), pp. 1851–1859.

[18] Patrick W Goodwill and Steven M Conolly. "Multidimensional x-space magnetic particle imaging". In: *IEEE Transactions on Medical Imaging* 30.9 (2011), pp. 1581–1590.

[19] Kuan Lu et al. "Linearity and shift invariance for quantitative magnetic particle imaging". In: *IEEE Transactions on Medical Imaging* 32.9 (2013), pp. 1565–1575.

[20] J Weizenecker et al. "Three-dimensional real-time in vivo magnetic particle imaging". In: *Physics in Medicine & Biology* 54.5 (2009), p. L1.

[21] A A Ozaslan et al. "Fully automated gridding reconstruction for non-Cartesian x-space magnetic particle imaging". In: *Physics in Medicine & Biology* 64.16 (Aug. 2019), p. 165018. DOI: 10.1088/1361-6560/ab3525.

[22] T Knopp et al. "Trajectory analysis for magnetic particle imaging". In: *Physics in Medicine and Biology* 54.2 (2008), p. 385.

[23] Tobias Knopp et al. "Model-based reconstruction for magnetic particle imaging". In: *IEEE Transactions on Medical Imaging* 29.1 (2010), pp. 12–18.

[24] Thomas Strohmer and Roman Vershynin. "A Randomized Kaczmarz Algorithm with Exponential Convergence". In: *Journal of Fourier Analysis and Applications* 15.2 (Apr. 2008), pp. 262–278. DOI: 10.1007/s00041-008-9030-4. URL: https://doi.org/10.1007/s00041-008-9030-4.

[25] Tobias Knopp and Thorsten M Buzug. *Magnetic particle imaging: an introduction to imaging principles and scanner instrumentation.* Springer Science & Business Media, 2012.

[26] J. Korhonen and J. You. "Peak signal-to-noise ratio revisited: Is simple beautiful?" In: *2012 Fourth International Workshop on Quality of Multimedia Experience.* 2012, pp. 37–38.

[27] A von Gladiss et al. "Hybrid system calibration for multidimensional magnetic particle imaging". In: *Physics in Medicine and Biology* 62.9 (Apr. 2017), pp. 3392–3406. DOI: 10.1088/1361-6560/aa5340.

[28] Alexander Weber and Tobias Knopp. "Reconstruction of the Magnetic Particle Imaging System Matrix Using Symmetries and Compressed Sensing". In: *Advances in Mathematical Physics* 2015 (Oct. 2015), pp. 1–9.

[29] T. Knopp and A. Weber. "Sparse Reconstruction of the Magnetic Particle Imaging System Matrix". In: *IEEE Transactions on Medical Imaging* 32.8 (2013), pp. 1473–1480.

[30] S. U. Dar et al. "Image Synthesis in Multi-Contrast MRI With Conditional Generative Adversarial Networks". In: *IEEE Transactions on Medical Imaging* 38.10 (Oct. 2019), pp. 2375–2388. ISSN: 1558-254X.

[31] C. Dong et al. "Image Super-Resolution Using Deep Convolutional Networks". In: *IEEE Transactions on Pattern Analysis and Machine Intelligence* 38.2 (2016), pp. 295–307. DOI: 10.1109/TPAMI.2015.2439281.

[32] Jelmer M. Wolterink et al. *Deep MR to CT Synthesis using Unpaired Data.* 2017. arXiv: 1708.01155 [cs.CV].

[33] Avi Ben-Cohen et al. "Virtual PET Images from CT Data Using Deep Convolutional Networks: Initial Results". In: *Lecture Notes in Computer Science* (2017), pp. 49–57. ISSN: 1611-3349. URL: http://dx.doi.org/10.1007/978-3-319-68127-6_6.

[34] Faisal Mahmood, Richard Chen, and Nicholas J. Durr. "Unsupervised Reverse Domain Adaptation for Synthetic Medical Images via Adversarial Training". In: *IEEE Transactions on Medical Imaging* 37.12 (Dec. 2018), pp. 2572–2581. ISSN: 1558-254X. URL: http://dx.doi.org/10.1109/TMI.2018.2842767.

[35] Yipeng Hu et al. "Freehand Ultrasound Image Simulation with Spatially-Conditioned Generative Adversarial Networks". In: *Molecular Imaging, Reconstruction and Analysis of Moving Body Organs, and Stroke Imaging and Treatment* (2017), pp. 105–115. ISSN: 1611-3349. URL: http://dx.doi.org/10.1007/978-3-319-67564-0_11.

[36] Phillip Isola et al. "Image-to-Image Translation with Conditional Adversarial Networks". In: *CVPR* (2017).

[37] S. Ilbey et al. “Fast System Calibration With Coded Calibration Scenes for Magnetic Particle Imaging”. In: *IEEE Transactions on Medical Imaging* 38.9 (2019), pp. 2070–2080. DOI: 10.1109/TMI.2019.2896289.